Available online at www.sciencedirect.com

ScienceDirect

Acta Materialia 87 (2015) 111–120

Acta MATERIALIA

www.elsevier.com/locate/actamat

The earliest stage of phase growth in sharp concentration gradients

B. Parditka,[a,b] J. Tomán,[a] C. Cserháti,[a] Zs. Jánosfalvi,[a] A. Csik,[c] I. Zizak,[d] R. Feyerherm,[d]
G. Schmitz[e] and Z. Erdélyi[a,*]

[a] *Department of Solid State Physics, University of Debrecen, P.O. Box 2, H-4010 Debrecen, Hungary*
[b] *Aix-Marseille Université, IM2NP, Faculté des Sciences de Saint-Jérôme case 142, 13397 Marseille, France*
[c] *Institute of Nuclear Research of the Hungarian Academy of Sciences (Atomki), P.O. Box 51, H-4001 Debrecen, Hungary*
[d] *Helmholtz-Zentrum Berlin für Materialien und Energie – Speicherring BESSY II, Albert-Einstein Str. 15, D-12349 Berlin, Germany*
[e] *Institute of Materials Science, University of Stuttgart, Heisenbergstraße 3, D-70569 Stuttgart, Germany*

Received 24 July 2014; revised 24 November 2014; accepted 27 November 2014

Abstract—Phase nucleation in sharp concentration gradient and the beginning of phase growth is investigated in Ni–Si and Co–Si systems experimentally and by computer simulation. We applied a combination of X-ray diffraction, four-wire resistance, grazing incidence X-ray fluorescence analysis and extended X-ray absorption fine structure spectroscopy in fluorescence detection with X-ray standing waves for the depth profiling of a-Si/Ni/a-Si (and a-Si/Co/a-Si) layers with nanometer resolution. We observed that a mixture of Ni and Si with a 2:1 composition ratio is formed at the interfaces during sample preparation, but its thickness was different at the a-Si/Ni and Ni/a-Si interfaces of opposite stacking. During annealing, the Ni_2Si crystalline phase formed, but, surprisingly, we observed that the thicker Ni_2Si layer grew faster than the thinner one. Similar peculiar behaviour was observed for the a-Si/Co/a-Si system. To clarify this situation, computer simulations were performed for both systems by using our new conceptual model (Erdélyi et al., 2012). This showed that the chemical thickness of the interfaces and the accelerated diffusion in the intermetallic phase probably play key roles in the earliest stages of growth.

Keywords: Solid-state reaction; Nucleation in a sharp concentration gradient; GIXRF; EXAFS; XRD

1. Introduction

The nucleation and early stage of phase growth during reactive diffusion have attracted considerable interest as these processes became particularly important with the downscaling of technical devices. Despite their importance, the atomistic details of nucleation and phase growth of intermetallic phases are not clear yet, especially in the presence of extreme composition gradients at interfaces when nucleation and phase growth are governed not only by thermodynamics but also by kinetics. According to well-elaborated ideas (see e.g. [1–3]), we can distinguish three types of nucleation mode: the polymorphic, transversal and total mixing schemes.

In the polymorphic mode, interdiffusion starts at the initial interface of the parent phases. The composition profile then becomes smooth enough to provide sufficient space for the formation of super critical nuclei of a new intermetallic phase. This phase nucleates by the local ordering of atoms; that is, without changing the composition profile. This polymorphic nucleation mechanism is physically plausible when the atomic mobilities of the two components in the compound nucleus differ by several orders of magnitude, which makes fast local ordering of atoms possible without changing the composition profile; moreover, significant solubility in the parent phases is required. In this nucleation scheme a sharp concentration gradient obviously hinders the nucleation process. This can be expressed by the nucleation barrier [1]:

$$\Delta G(r) = \Delta G^{\text{classic}} + \gamma(\text{grad } c)^2 r^5 \qquad (1)$$

where $\Delta G(r)$ is the change in Gibbs free energy due to the formation of a cubic nucleus of size $2r$ or a spherical nucleus of radius r; γ is a coefficient that is positive in the polymorphic scheme; c is the local composition gradient; and $\Delta G^{\text{classic}}$ is the change in Gibbs free energy due to phase formation in the classical theory of nucleation.

If the solubility of the terminating phases is too restricted, a polymorphic nucleation mode is not possible. Instead, intermetallic embryo construction may proceed through an exchange of matter between the nucleation zone and the surrounding in directions perpendicular to grad c, i.e. atomic transport is operating in directions perpendicular

---

[*] Corresponding author; e-mail: zoltan.erdelyi@science.unideb.hu
URL: http://web.unideb.hu/zerdelyi.

http://dx.doi.org/10.1016/j.actamat.2014.11.048
1359-6462/

to grad c. This is called the transversal mode of nucleation. In the case of a sharp concentration gradient, this nucleation scheme also predicts initial suppression of the nucleation event by an increase of the nucleation barrier ($\gamma > 0$ in Eq. (1)).

If, however, the atomic mobility of each component in the new phase is much greater than in the parent phases, complete interdiffusion, on the embryo scale, in the direction of grad c is expected for nucleus formation. This yields no concentration gradient in the ordered embryo and is consequently the most stable stoichiometric phase. This scheme is designated the total mixing mode of nucleation. This scheme does not predict any hindering of the nucleation event in a sharp concentration gradient and the driving force for nucleation is even increased by the composition gradient ($\gamma < 0$ in Eq. (1)).

Sound experimental verification of the different nucleation schemes are extremely rare (e.g. [2]) as these requires technique with nano- or even atomic scale resolution.

Even less is known about the initial growth before steady-state composition profiles are established. In this work we focus specifically on this intermediate stage between nucleation and the latter steady state of diffusion, which would only result in linear or parabolic growth of the reaction products.

We applied a large variety of experimental techniques and computer simulation based on a new conceptual model of calculating intermetallic phase growth [4] to investigate the nucleation and growth of intermetallic phases in sharp concentration gradients.

Our team recently introduced the combination of grazing incidence X-ray fluorescence (GIXRF) and extended X-ray absorption fine structure (EXAFS) spectroscopy in fluorescence detection with the X-ray standing wave (XSW) technique to monitor compound phase formation and growth with nanometer resolution, namely the formation of CoSi in the Co–Si system [5]. The experiment reported in this paper represents a second example. However, we not only repeat the previous experiment in another system, but further develop the evaluation method by correlating the results of independent GIXRF and EXAFS measurements. From both analyses we are able to determine the ratio of the fluorescent signals stemming from the Ni_2Si layers and the Ni layer (I_{Ni_2Si}/I_{Ni}) as a function of annealing time, which increases the reliability. We observe that Ni_2Si is formed just at the interfaces in accordance with literature results [6], though its thickness was different at the a-Si/Ni and Ni/a-Si stackings. Surprisingly, we also observe that the thicker Ni_2Si layer subsequently grows faster than the thinner one during heat treatment.

As a consequence of this surprising observation, we have reviewed our results obtained previously in the a-Si/Co/a-Si system [5]. The thickness of the CoSi phases was different at the a-Si/Co and Co/a-Si interfaces also in this case, and interestingly we further found that the thicker CoSi phase grew faster. To clarify this situation, we will present computer simulations for both systems based on our recent model [4].

Accordingly, the present paper is organized as follows: description of the experiments, details of the computer simulation method, the obtained results, comparison of the experimental and computer simulation results, discussion and conclusions.

2. Experiments

Ta(5 nm)/a-Si(12 nm)/Ni(10 nm)/a-Si(14 nm)/Ta(30 nm)/SiO_2(substrate) samples were prepared by magnetron sputtering (the same technique as in Ref. [7]). Tantalum was chosen as the waveguide (mirror) layer since on the one hand it fulfills the requirements for a good mirror material (high atomic number) and on the other hand Ta/Si contacts remain intact during heat treatment (no reaction or significant diffusion take place). The samples were annealed for different times at 463 and 503 K under high vacuum ($\approx 10^{-5}$ Pa) conditions. Note that, on the basis of previous reports, we expected measurable Ni_2Si phase formation (the first phase to grow) in this temperature range. Ni_2Si and Ni standards were also prepared in order to perform a linear combination fit to EXAFS data. Moreover, $[Ni_{20\ nm}/Si_{20\ nm}] \times 10$ multilayers were deposited onto sapphire substrates for a combination of X-ray diffraction (XRD) and four-wire resistance experiments.

The graded-crystal monochromator beamline KMC-2 (Bessy II at Helmholtz-Zentrum Berlin) was used to set up the in-depth nanoprobe EXAFS system. The X-ray beam in the energy range of 79 keV was monochromatized by the double-crystal monochromator and collimated in both directions using two slit systems. The X-ray beam is condensed to the sample using a toroidal mirror. Since the convergent beam passes through the monochromator, a special Si–Ge graded crystal was used to provide the energy bandwidth of 1.5 eV. The beam size on the sample position was 100 μm horizontal and 700 μm vertical. The beam divergence was determined to be of order of 20 arc sec by rocking curve measurements of a Si (1 1 1) reference crystal. The total flux in the spot was in the range of 10^9 phot s^{-1} @ 100 mA. Ring current varied between 150 and 290 mA. The beamline monochromator, stabilized by the MOSTAB feedback system for EXAFS measurements, provides root mean square intensity variations of the order of 1.7×10^{-3} across the entire energy range. Control software was used to provide simultaneously an energy scan of the monochromator and an angular scan of the sample.

For every sample,simultaneous reflectometry and GIXRF measurements were performed to measure the composition profile of the multilayer sample. A PIN photodiode detector was used to measure the reflected (diffracted) beam. An energy-dispersive detector (Röntec X-Flash, 170 eV resolution) was used to record the fluorescence spectrum of the sample. The sample and both detectors were mounted on independent Huber goniometers with a mutual z-axis. The sample was mounted vertically, so that the rotation around the z-axis provided the regulation of the incident angle. The energy-dispersive detector was mounted 10 mm above the sample surface oriented normally to the surface.

An activation energy above the K absorption edge of Ni (8.33 keV) was used. Knowing the distribution of Ni in the sample, the angle of incidence was tuned between 0 and 0.6° to produce standing wave patterns with a maximal electric field at specific depth positions in the sample. EXAFS experiments, which detected the fluorescence signal, were performed for standing wave patterns, with the maximal field amplitude in the middle of the Ni layer and at each interface. Since EXAFS scans were performed by varying the activation energy in the range of 8.3–8.6 keV, it was necessary to tune the incidence angle during the scan in order to keep the standing wave pattern constant during each EXAFS scan. The energy step in the near-edge region was 5 eV; this was changed after 50 eV to a constant q step to ease the EXAFS evaluation. The acquisition time was 1 s in the near-edge region and was increased proportionally to q^2 up to 5 s at the end of the scan (600 eV above the edge). This was done to diminish the statistical fluctuations at higher q values, since data (and noise) are weighted with q^2 in EXAFS evaluation.

EXAFS measurement without using the waveguide structure would give an average signal from the complete layer, i.e. the measurement would not be depth resolved. As most Ni atoms are in the middle of the layer, pure Ni would dominate the signal. By using the waveguide structure, however, the measurement is depth sensitive, which allows the signal from the interfaces to be emphasized.

In situ XRD measurements were performed at the high flux hard X-ray MAGS (7TMPW) beamline (Bessy II at Helmholtz-Zentrum Berlin) [8] in a vacuum ($\sim 10^{-6}$ Pa) to monitor the formation of the crystalline Ni_2Si intermetallic phase. During the XRD measurements, four-wire resistance measurements were also performed. The temperature was controlled with ±1 K accuracy during the heat treatment. Symmetrical scans between 0° and 90° of the scattering angle 2Θ were performed at 12 keV. Isothermal heat treatments were performed in the range 467–503 K.

2.1. Profile reconstruction – GIXRF

The advantage of XSW techniques has already been discussed in detail in Refs. [9,10,5]. Here we briefly summarize only the basics of the technique.

XSW-based techniques offer elemental depth profiling with nanometer resolution. One of the possible geometries is to put the sample layer in the space between two reflecting (mirror) layers. The trapped incident beam will be bounced back and forth on the waveguide mirror layers and interfere with itself, so standing waves of the electric field will form at specific incidences (see Fig. 1).

The angles satisfying resonance conditions can be written as:

$$\Theta_m = (m+1)\pi/kW \qquad (2)$$

where k is the absolute value of the wave vector of the X-ray, W is the width of the cavity (distance between the waveguide layers) and m is an integer.

The square of the developing electric field at a given depth can be regarded as the intensity of the primary X-ray beam. When we place layered materials – including an absorbing one (in our case a-Si/Ni/a-Si triple layer) – between the mirror layers, the fluorescence intensity is going to be proportional to the square of the electric field at the absorbing layer position and the fluorescence signal will come from that part of our structure where the absorbing layer and the anti-nodal part, i.e. the electric field intensity of the XSW, overlaps [9,10,5,11,12]. Changing the angle of incidence, the tuning to the different modes of the XSW is possible and so the positions of the anti-nodal parts can be positioned to the depth of interests.

The intensity of the fluorescence signal is therefore proportional to the square of the electric field generated by the incoming X-ray beam [5]:

$$I(\Theta) \propto \int_0^L c(x)E^2(\Theta,x)\mathrm{d}x \qquad (3)$$

where c is the atomic fraction of the element which we are interested in, E is the amplitude of the electric field, L is the thickness of the sample – including the waveguide layers – and Θ is the incident angle. On the basis of this equation, therefore, it is possible to calculate the fluorescence radiation intensity vs. the angle of incidence, which provides the possibility of reconstructing the composition profile of the absorbing element. In order to use this formula, E has to be calculated. This is based on the application of Fresnel equations, modified to account for interface imperfections, which describe the reflection and transmission of an electromagnetic plane wave incident at an interface between two optically dissimilar materials [13–15].

Therefore, supposing a composition profile, it is possible to calculate the electric field and so also the fluorescence intensity. The calculated fluorescence intensity curve can be compared to the measured one. By iterative fitting of

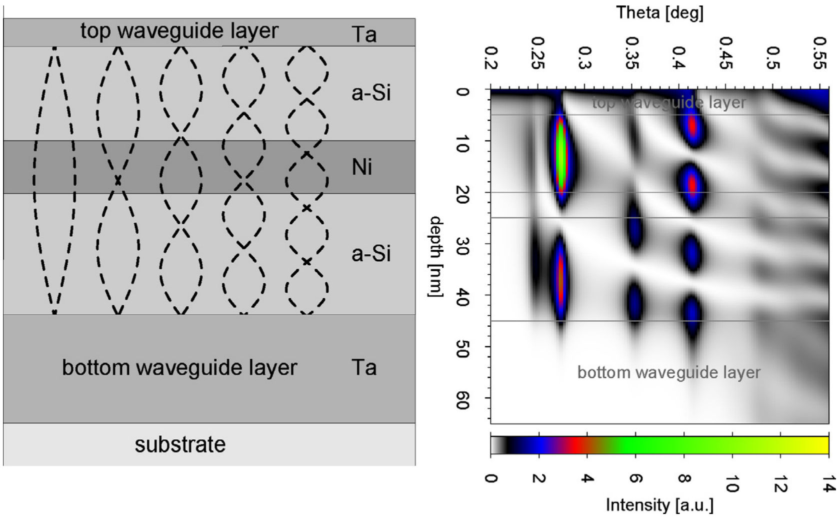

Fig. 1. (a) Waveguide sample structure. The a-Si/Ni/a-Si trilayer is the sample investigated. The schemes of the first five transversal modes of the electric field (TE) are also illustrated. (b) Intensity plot of the calculated electric field (photon energy: 8.40 keV). The different TEs as a function of the angle of incidence are displayed.

the measured and simulated intensities, the composition profile can be reconstructed. The reconstruction software was developed by our group [5].

2.2. EXAFS

When the energy of the incident X-ray photon equals or exceeds the ionization energy, an electron may be released, ejected from the atom. In the X-ray absorption spectrum, the onset of this phenomenon is marked by an abrupt drop that is called the absorption edge. These edges are sorted by the quantum numbers of the electrons in the ground state.

The EXAFS is the oscillating part of the recorded X-ray absorption spectrum that starts from the absorption edge and finishes about 1000 eV above. Structural information, such as numbers and distances of the neighbouring atoms and some of their properties, can be extracted from this oscillating part. In brief, a tranche of chemical information becomes available with the help of this powerful probe.

The photoelectrons ejected from the absorber atoms interfere with scattering centres in the surroundings, i.e. the neighbouring atoms. The obtained EXAFS spectra are thus the result of the interference of the ejected and scattered photoelectrons. The details of the interference depend on the distance and the atomic number of the neighbouring atoms.

We define the EXAFS fine-structure function $\chi(E)$ as [16]

$$\chi(E)=\frac{u(E)-u_0(E)}{\Delta u_0(E)} \tag{4}$$

Here $u(E)$ is the measured absorption coefficient. In fluorescence detection

$$u(E)\propto\frac{I_f}{I_0} \tag{5}$$

where I_f is the monitored intensity of a fluorescence line associated with the absorption process and I_0 is the X-ray intensity incident on a sample. $u_0(E)$ is a smooth background function representing the absorption of an isolated atom and Δu_0 is the measured jump in the absorption coefficient $u(E)$ at the threshold energy E_0. The primary quantity for EXAFS is then expressed as $\chi(k)$, the oscillations as a function of photo-electron wave number, where

$$k=\sqrt{\frac{2m(E-E_0)}{\hbar^2}} \tag{6}$$

with m being the electron mass and $\hbar$ being Planck's constant over 2π.

The different frequencies apparent in the oscillations of $\chi(k)$ correspond to different near-neighbour coordination shells, which can be described and modelled as the sum of neighbourhoods:

$$\chi(k)=\sum_j\frac{N_jf_j(k)e^{-2k^2\sigma_j^2}}{kR_j^2}\sin\left[2kR_j+\delta_j(k)\right] \tag{7}$$

where $f(k)$ and $\delta(k)$ are the scattering properties of the neighbouring atoms, N is their number, R is their distance to the primary scattering centre and σ^2 is the disorder in the neighbour distance. Though somewhat complicated, this EXAFS equation allows us to determine N, R and σ^2, knowing the scattering amplitude $f(k)$ and the phase shift $\delta(k)$. Furthermore, since these scattering factors depend on the atomic number Z of the neighbouring atom, EXAFS is also sensitive to the species of the neighbouring atoms.

To measure an absorption spectrum, one has to vary the energy of the incident beam. This would change the electric field pattern. However, in order to gain information from a given depth, one must keep the electric field pattern constant. In order to achieve this, simultaneous corrections of the incident angle are necessary. Control software was used to simultaneously provide this energy scan of the monochromator and the angular scan of the sample.

The position of the sampling volume could be changed by changing the transversal mode of the electric field pattern [17,5].

3. Computer simulations

In Ref. [4] we introduced a concept for describing intermetallic phase formation and growth in a solid-state reaction. In this concept, phases form automatically as thermodynamics dictates – via chemical potentials – and grow. Unlike in earlier approaches, it is not necessary to pre-define any Gibbs surfaces or make other ad hoc assumption about reaction layers.

Note that other authors has also tested and used our conceptual model with success (see e.g. [18]).

3.1. Basic equations

The basic equations can be found in Ref. [4]. However, for clarity, we report them here and write them in a modified version that is more suitable for the current computation purposes. Moreover, we suppose that the sinks and sources of vacancies are effective enough to maintain the equilibrium concentration of vacancies everywhere all the time. Accordingly, unlike in Ref. [4], the vacancy-related quantities – such as chemical potential, composition, sinks and source term – do not appear in the equations. Furthermore, for the sake of simplicity, we also suppose that the atomic volumes of the constituents are equal, consequently the total material density is constant. There are no stress effects.

As a result, the equations become reasonably simple, but are still highly suitable for our purposes.

3.1.1. Continuity equation

In order to calculate the change of composition in time and space, the following equation is used [4]:

$$\frac{\mathrm{D}c_i}{\mathrm{D}t}=-\frac{1}{\rho}\operatorname{div}'\vec{j}_i \quad \text{for } i=1,\ldots,n \tag{8}$$

where $\mathrm{D}/\mathrm{D}t$ is known as a substantial (or material) derivative. It gives the rate of change of any scalar quantity seen at a point which follows the motion of the material coordinate system. $\vec{j}_i$ is the flux of component i, ρ is the total material volume density, c_i is the atomic fraction of component i and div' indicates the divergence calculated in the material coordinate system (see e.g. [4]).

The flux of component i can be written as [4,19]

$$\vec{j}_i=-\rho D_i^*\frac{c_i}{RT}\operatorname{grad}'\mu_i \quad \text{for } i=1,\ldots,n \tag{9}$$

where D_i^* denotes the tracer diffusion coefficient, R is the ideal gas constant, T is the absolute temperature, grad′ indicates the gradient calculated in the material coordinate system (see e.g. [4]) and μ_i is the chemical potential of component i.

Note that as we have supposed the ρ to be constant everywhere all the time, it vanishes by substituting Eq. (9) into Eq. (8). Accordingly, it is not necessary to calculate ρ.

It is worth mentioning that these equations are formulated for the so-called diffusion controlled regime of phase growth. In the interface-controlled regime, an equation different from Eq. (9) should be used at the phase boundaries. However, as was shown in Ref. [4] for the model used here, the silicide phase forms automatically as the thermodynamics dictates without any further supposition (pre-defined interfaces, etc.), and this is the most important feature we needed. A modification of the model for interface control regime is beyond the scope of this paper.

3.1.2. Chemical potentials

The solubility is highly asymmetric in both the Ni–Si and Co–Si systems – the solubility of Si in Ni or Co is about 10%, but Ni and Co are both practically insoluble in Si [20]. Moreover, the existence range of the intermetallics is quite narrow for Ni_2Si and CoSi [20].

Corresponding to this thermodynamic situation, we perform a model calculation for a binary system in which one intermetallic phase forms in equilibrium with the terminal ideal solid solutions.

The Gibbs energies for a solid solution (SS) g^{SS} and an intermetallic (IM) phase g^{IM} for a regular binary system can be modelled [4,21] as:

$$\begin{aligned} g^{SS} &= G_A c + G_B(1-c) + RT[c\ln c + (1-c)\ln(1-c)] \\ &\quad + Lc(1-c) \\ g^{IM} &= g_0 + V(c-c_m)^2 \end{aligned} \tag{10}$$

Here G_i is the Gibbs energy of the pure component $i = (A, B)$, c is the atomic fraction of component A, L is an interaction parameter (in general, composition and temperature dependent), c_m is the stoichiometric concentration of component A in the intermetallic phase, and g_0 and V are parameters by which the Gibbs energy of the intermetallic phase can be adjusted.

Note that in Ref. [4] the same g^{SS} was used on both sides of the phase diagram. That simple scheme, however, is not suitable to account for the Gibbs energy functions, the asymmetric solubility and the narrow existence range of intermetallics in the Ni–Si and Co–Si systems. We therefore use in this work two different parameter sets on the two sides of the phase diagram to calculate g^{SS}.

The chemical potentials of component A are

$$\begin{aligned} \mu_A^{SS} &= G_A + RT\ln c + (1-c)^2\left(L + c\frac{\partial L}{\partial c}\right) \\ \mu_A^{IM} &= -g_0 + V\left(-c^2 + c_m^2 + 2c - 2c_m\right) \end{aligned} \tag{11}$$

Again, there are two μ_A^{SS} functions, as G_A, G_B and L have different values on both terminating sides of the phase diagram. The Gibbs potentials and the calculated chemical potential of Ni in the Ni–Si system are shown in Fig. 2.

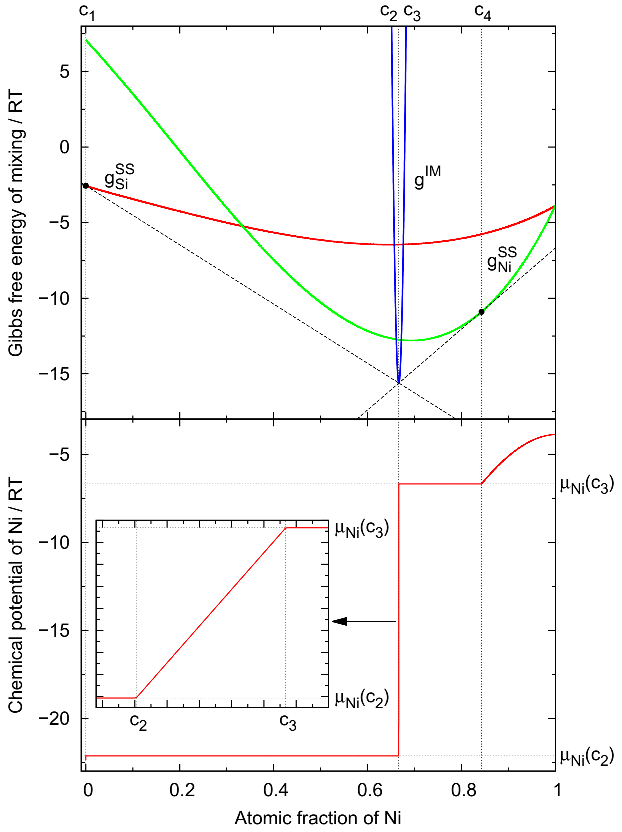

Fig. 2. Upper panel: Gibbs potentials for Ni-rich solid solution (g_{Ni}^{SS}), Si-rich solid solution (g_{Si}^{SS}) and Ni_2Si intermetallic (g^{IM}) phases. $c_1(\approx 10^{-6})$ and $c_4(\approx 0.843)$ are the equilibrium compositions in the solid solutions, whereas $c_2(\approx 0.6665)$ and $c_3(\approx 0.6667)$ are at the phase boundaries. Lower panel: chemical potential of the atomic component of Ni in the Ni–Si system. The inset shows the chemical potential function in the intermetallic phase magnified for better visualization.

3.2. Input parameters and algorithm

We normalize the Gibbs energy – and also the chemical potential – by RT. Accordingly, the temperature does not have to be set directly, i.e. there are only two values for G_A, G_B and L (for the two sides of the phase diagram), so g_o, V and c_m are the input parameters required to construct the chemical potential function (see Table 1).

We suppose that D^* has the same value for both components and, furthermore, is composition independent within any of the phases (the solid solutions and the intermetallic phase). The latter is plausible as the composition range for both the intermetallics and the solid solutions is quite narrow. The value of D^*, however, is allowed to vary between the different phases.

Eqs. (8) and (9) are solved by the standard numerical method.

4. Results and discussion

4.1. Experimental observations

Samples as-deposited and annealed for 4 h 30 min, 4 h 45 min and 5 h 30 min at 503 K were measured. As a dem-

Table 1. Input parameters for Gibbs potentials ($T = 500$ K).

	Ni–Si		Co–Si	
G_A^1/RT	-3.88[a]	FCC Ni	-2.75[a]	HCP Co
G_B^1/RT	-2.55[a]	DIA Si	-2.55[a]	DIA Si
G_A^2/RT	-3.88[a]	FCC Ni	-2.75[a]	HCP Co
G_B^2/RT	7.09[a]	FCC Si	-2.55[a]	DIA Si
L^1/RT	$0.25L^{(Ni)}_{Ni,Si}/RT$[b]		$0.3\,L^{(Co)}_{Co,Si}/RT$[c]	
L^2/RT	$1.0L^{(Ni)}_{Ni,Si}/RT$[b]		$0.6\,L^{(Co)}_{Co,Si}/RT$[c]	
c_m	0.6666		0.5	
g_0/RT	-15.61[d]		-14.51[d]	
V/RT	10^5		10^4	

[a] $(G - H_{SER})$ values from the SGTE database [22] divided by RT.

[b] $L^{(Ni)}_{Ni,Si} = -208234.46 + 44.14177\,T - 108533.44(c_A - c_B)$ [23].

[c] $L^{(Co)}_{Co,Si} = -199795.7 + 35.01457\,T + (-3322.1 + 9.000271\,T)(c_A - c_B)$ [24].

[d] $g_0 = c_m G_A^1 + (1 - c_m)G_B^1 + H_f$ H_f enthalpy of formation from Ref. [25].

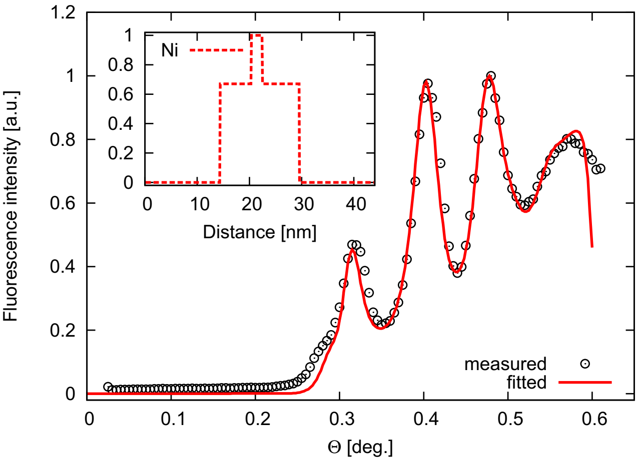

Fig. 3. Measured data (annealed at 503 K for 4 h 30 min) obtained from GIXRF measurements (black circles) and the fitted counterpart (red line). The inset shows the corresponding reconstructed composition profile of *Ni*. (For interpretation of the references to color in this figure legend, the reader is referred to the web version of this article.)

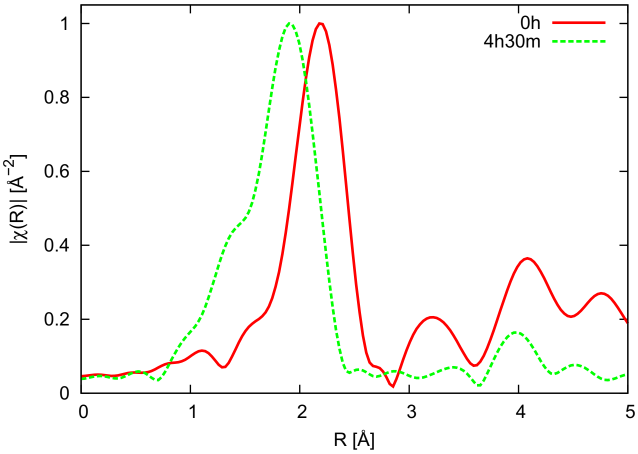

Fig. 4. Magnitudes of the Fourier transforms of $\chi(k)$ for the as-prepared and annealed (for 4 h 30 min) specimens plotted on a normalized scale.

onstration, Fig. 3 shows a measured and a calculated GIXRF intensity curve. The inset shows the corresponding reconstructed composition profile.

We found that, even in the as-deposited sample, Ni and Si atoms in a 2:1 composition ratio (either crystalline or amorphous) are present on both sides of the Ni layer. Such a phenomenon is not uncommon for samples prepared by sputtering techniques, for which several nanometres thick mixed layers were reported directly after deposition [26–28].

We performed EXAFS measurements by fluorescence detection across the nickel absorbing edge to obtain more information about the chemical state of the species (number of nearest neighbours, atomic distances, etc.) The raw EXAFS data had to be calibrated by the known value of the absorption edge of Ni. For better statistics, samples were measured several times, then the data of the separate measurements were aligned to that edge and averaged.

In Fig. 4 the magnitudes of the Fourier transforms of the as-prepared and annealed (4 h 30 min) specimens are plotted in a normalized scale. The relative average atomic distances can easily be read from this kind of plot. By annealing, the position of the most intense peak shifts towards a smaller value of *R*, which means that the nearest-neighbour distance has decreased. This is in agreement with the expectation that Ni_2Si intermetallic phase forms at the Ni/Si interfaces during heat treatment. It also indicates that, in the as-deposited sample at the interfaces, there are only disordered mixtures, possibly even amorphous, of Ni and Si atoms with a ratio corresponding to Ni_2Si. This is in very good agreement with the results of the XRD–four-wire resistance measurements. For the latter we needed isolating substrates; accordingly, the samples were deposited onto Al_2O_3 substrates in this case. In the diffraction pattern recorded in the as-deposited samples, only an Ni(1 1 1) peak is present. At the beginning of the heat treatment the intensity of this Ni(1 1 1) peak decreases, before later peaks corresponding to the Ni_2Si phase start to grow. In accordance with this observation, the resistance of the sample increases first and then, just as the Ni_2Si peak appears, starts to decrease (see Fig. 5). This can be explained by the assumption that first the amount of the low-resistance crystalline Ni decreases while a disordered mixture of Ni and Si with high resistance forms. Later, this mixture crystallizes into Ni_2Si phase, which has low resistance and keeps growing.

In Fig. 6 the result of the linear combination fit of the absorption coefficient data (see Eq. (5)) of a sample

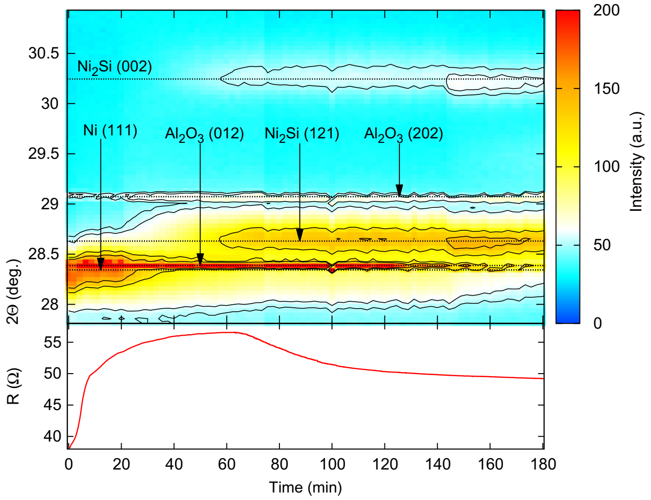

Fig. 5. Diffraction pattern (upper panel) and four-wire resistance curve (lower panel) recorded in situ in Ni/Si multilayer during annealing at 467 K. At the beginning of the annealing the Ni(1 1 1) peak decreases (i.e. becomes narrower and less intensive – see the colour change apart from the Al_2O_3 substrate signal) and the resistance increases. Then Ni_2Si(0 0 2) and Ni_2Si(1 2 1) peaks start to grow and the resistance starts to decrease. Note that the constant Al_2O_3 peaks are from the substrate.

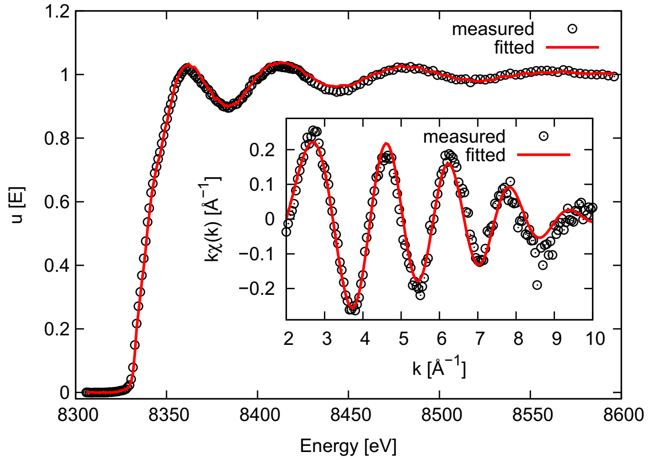

Fig. 6. Results of fits of the EXAFS data: linear combination fit (see in the text) of the absorption coefficient data at $\Theta = 0.4285°$. The weights of the Ni and Ni_2Si standard spectra were 0.113 and 0.887, respectively. The inset shows the fit by the k-weighted EXAFS equation using the crystallographic data of Ni_2Si from Ref. [30] (the sample annealed at 503 K for 4 h 30 min).

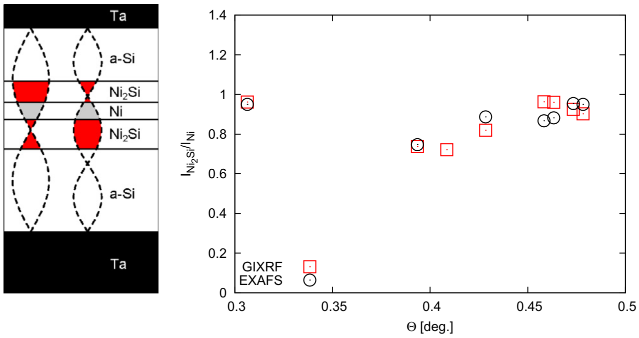

Fig. 7. (a) Schematic showing the source of the fluorescence signal for two different transversal modes of the electric field. The total fluorescence signal originates from the volume where the pure Ni (grey) and the Ni_2Si (red) product layers overlap with the antinodal parts of the generated XSW. The ratios plotted in (b) come from the weighted values of these areas. (b) I_{Ni_2Si}/I_{Ni} ratio for the sample annealed at 503 K for 4 h 30 min obtained from the GIXRF analyses and the linear combination fit of the EXAFS data. (For interpretation of the references to colour in this figure legend, the reader is referred to the web version of this article.)

annealed at 503 K for 4 h 30 min is plotted. Linear combination fit means that we also performed measurements on Ni and Ni_2Si standards, which were prepared in the same manner as the specimens themselves. The ATHENA-ARTEMIS software package [29] has the capability of fitting a linear combination of standard spectra (Ni and Ni_2Si) to an unknown spectrum. By fitting each intermediate spectrum as a linear combination of the standard spectra, we deduce the relative quantities of crystalline Ni and ordered Ni_2Si in the annealed heterogeneous samples.

In order to further strengthen the idea that the product phase is indeed Ni_2Si, the data were also fitted by the k-weighted EXAFS equation (k times Eq. (7)) up to $R = 5$ Å ($k = 8.5$ Å^{-1}) using the ATHENA-ARTEMIS software package (see the inset in Fig. 6). This analysis confirmed that Ni_2Si is formed at the interfaces during annealing while only a disordered mixture of Si and Ni atoms with 2:1 composition ratio exists at the interfaces in the as-prepared samples. We found that after 5 h 30 min annealing at 503 K, almost the whole Ni layer transformed to the Ni_2Si intermetallic phase. This is in agreement with the GIXRF results.

The result of the EXAFS analysis was used to refine and confirm the sample structure to fit the fluorescence curves.

To increase the reliability of the combined GIXRF-EXAFS analysis, we further developed the evaluation by correlating independent GIXRF and EXAFS measurements.

Both in the GIXRF and EXAFS measurements the total fluorescence signal originates from the volume where the pure Ni and the Ni_2Si product layers overlap with the antinodal parts of the generated electric field (see Fig. 7). This means that the ratio of the signal stemming from the Ni_2Si layers and the Ni layer (I_{Ni_2Si}/I_{Ni}) can be deduced from the GIXRF measurements, since it is equal to the overlapping area of the electric field and the Ni_2Si layers times 2/3 (only 2/3 of the atoms in Ni_2Si are Ni) divided by the overlapping area of the electric field and the Ni layer.

On the other hand, I_{Ni_2Si}/I_{Ni} originating from the EXAFS measurements is equal to the ratio of the weighting factors used in the linear combination fit presented in Fig. 6.

I_{Ni_2Si}/I_{Ni} was determined for different transversal modes of the electric field and as a function of annealing time from both GIXRF and EXAFS, as shown in Fig. 7. The results of the two independent experimental methods are in perfect agreement.

In summary, for fitting GIXRF data we had to assume that a mixture of Ni and Si atoms with a 2:1 ratio (either amorphous or crystalline) had already formed on both sides of the pure Ni during sample preparation. XRD and four-wire resistance measurements showed that these layers are disordered Ni_2Si. This mixture transforms into Ni_2Si intermetallic phase and grows continuously in time

Table 2. Phase thicknesses on the two sides of the metal layer vs. time for the a-Si/Ni/a-Si system annealed at 503 K and the a-Si/Co/a-Si system annealed at 500 K.

	Time (h)	a-Si/Metal (nm)	Metal/a-Si (nm)	**Difference (nm)**
Ni–Si	0	5.4	6.2	**0.8**
	4.5	6.0	7.1	**1.1**
	4.75	6.6	8.1	**1.5**
	5.5	6.7	8.5	**1.8**
Co–Si	0	0.0	0.9	**0.9**
	1	0.5	2.5	**2.0**
	3	1.5	3.5	**2.0**

during the heat treatment (see Table 2). This was not surprising, though we found a peculiar behaviour in the time evolution of the Ni_2Si phase.

First, the thickness of the Ni_2Si mixture is different at the a-Si/Ni and Ni/a-Si interfaces of the as-deposited sample, being thicker at the Ni/a-Si interface by 0.8 nm (see Table 2). This can be explained naturally by the so-called dynamic segregation [31]: when Ni is deposited on top of Si, the Si atoms move towards the free surface due to their tendency to segregate to the Ni surface. However, when Si atoms are deposited onto Ni, the Si atoms stay on top while the Ni atoms remain below. This means that in the first stacking sequence the dynamic segregation enhances, whereas in the second it hinders, the formation of the pre-nucleation mixture (the mixture of Ni and Si in a 2:1 ratio).

Surprisingly, however, we observed that the thicker phase grows faster than the thinner one during annealing (see Table 2), although the reverse is be expected. If we suppose that the width of the intermetallic phase (W) increases proportionally to the square root of time ($W \propto \sqrt{t}$, often referred as parabolic kinetics or diffusion control), the growth rate should be inversely proportional to the width of the intermetallic phase $\left(\frac{dW}{dt} \propto 1/\sqrt{t} \propto 1/W\right)$, which would only decrease within the difference of the widths of the intermetallic layers. If, however, we suppose that $W \propto t$ (often referred as linear kinetics or interface control), it follows that $\frac{dW}{dt} = const$, which would result in no change in the absolute difference between the widths of the intermetallic layers.

Faced with this unexpected observation, we reviewed our results obtained in the a-Si/Co/a-Si system [5] and checked them in an independent experiment, as we had not paid particular attention to the kinetics earlier, focusing instead on the methodical aspects. Interestingly, we observed the same tendency: initially the thickness of the pre-nucleation mixture was 0 at the a-Si/Co interface and 0.9 nm at the Co/a-Si interface, meaning that the difference in thickness was 0.9 nm (see Fig. 3 in Ref. [5]). After heat treatment for 1 h the difference had increased to 2.0 nm (not published in Ref. [5]), and remained at this level after 3 h (see Fig. 3 in Ref. [5]; see also Table 2).

4.2. Computer simulations

To understand this unexpected growth behaviour, we performed computer simulations with the model described in Section 3.

We created a B/A/B triple layer, where B and A correspond to Si and Co or Ni, respectively. To simulate the Co–Si system, the interface on the left-hand side was supposed to be sharp initially, whereas on the right-hand side some pre-existing intermetallic phase was assumed. For the Ni–Si system, pre-existing intermetallic phases were assumed at both interfaces but with different thicknesses, in accordance with the experiments. First, we supposed that D^* had the same value in each phase (parent phases A and B, and the intermetallic phase). In this case, the computer simulations showed that the difference in width of the intermetallic phases at the two interfaces only decreased with time – as expected on the basis of parabolic or linear growth.

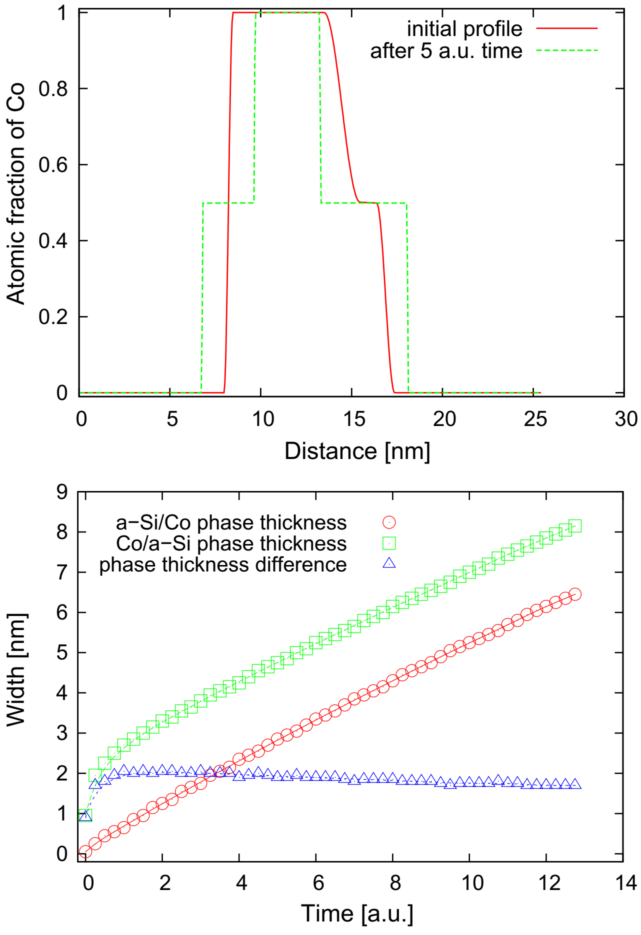

Fig. 8. (a) Composition profiles of the initial state ($t = 0$) and after some time ($t = 5$ a.u.) for the Co–Si system. Initially the left phase boundary is 0.5 nm thick, without any intermetallic phase. On the right side of the pure Co phase there is already a 0.9 nm thick intermetallic phase, with 2.0 and 1.0 nm thick diffused boundaries on its left and right sides, respectively. (b) The change in the widths of phases on the two sides of the initially pure Co phase and their difference. In accordance with the literature data, the diffusion is speeded up in the CoSi intermetallic phase (by multiplying D by 500) and in the Si-rich side of the phase diagram (by multiplying D by 1000).

However, it is not realistic to suppose that all the interphase boundaries (pure Si/pure Co, pure Co/CoSi and CoSi/pure Si, as well as pure Si/Ni_2Si, Ni_2Si/pure Ni, pure Ni/Ni_2Si and Ni_2Si/pure Si) are infinitely sharp after deposition. Therefore, to be more realistic, we performed calculations with initial composition profiles in which the boundaries on the right-hand side of the pure metallic layer were more diffuse than on the left-hand side. This way, the

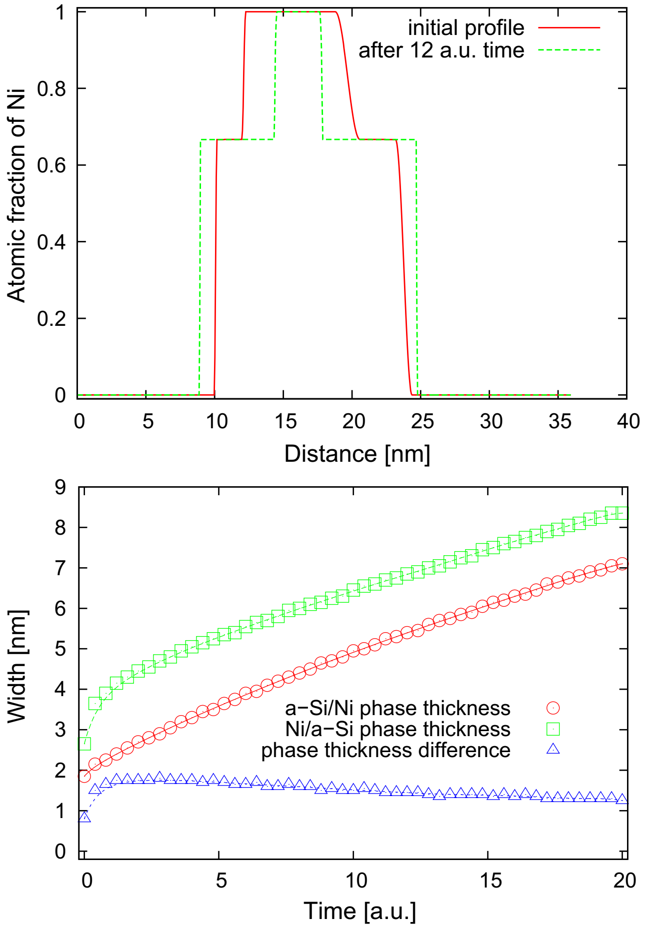

Fig. 9. (a) Composition profiles of the initial state ($t = 0$) and some time ($t = 12$ a.u.). Initially there is a 0.2 nm thick diffused part, then a 1.8 nm thick intermetallic phase and a 0.3 nm thick diffused part on the left side of the pure Ni phase. On the right side of the 6.5 nm pure Ni phase there is a 1.8 nm thick diffused part, then a 2.6 nm thick Ni_2Si phase and a 1.2 nm thick diffused part again until the pure Si phase. (b) The change in the widths of phases on the two sides of the initially pure Ni phase and their difference over time. The diffusion is speeded up in the Ni_2Si intermetallic phase (by multiplying D by 100) and in the Si-rich side of the phase diagram (by multiplying D by 1000).

initial difference between the widths of phases indeed increased temporarily, though the magnitude of the effect was much smaller than found in the experiment. After reaching a maximum difference shortly after the beginning, the asymmetry in the growth rate reversed and the difference started to decrease rapidly.

With a third simulation, however, supposing realistic material-dependent D^* values, i.e. the diffusion is 5–5,000 times faster in the intermetallic layer and 1000–10,000 times faster in the a-Si layer than in the metallic layer, we were able to reproduce the experimental observations well, as exemplified in Figs. 8 and 9. The difference in width between the intermetallic layers increases from 0.9 nm (Co–Si) and 0.8 nm (Ni–Si) to the experimentally observed values of 2.0 nm (Co–Si) and 1.8 nm (Ni–Si), this difference subsequently decreasing very slowly in time. Note that we did not intend to fit the experimental curves. As a proof of principle, the computer simulations with realistic input parameters reproduce the experimental observation.

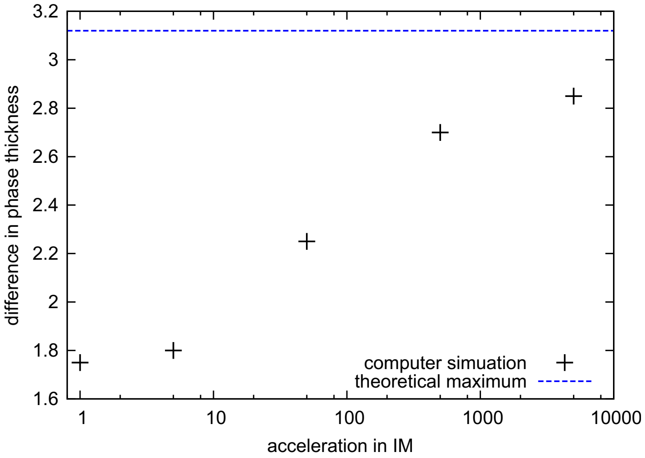

Fig. 10. Maximum differences between the thicknesses of the two intermetallic layers at different accelerations of mobilities in the CoSi intermetallic phase (1, 5, 50, 500, 5000). The blue dashed line shows the calculated maximum difference (see text). The initial interface thicknesses were: a-Si/Co, 0.5 nm; Co/CoSi, 3 nm; CoSi/a-Si, 1.5 nm. The initial phase thickness at the Co/a-Si interface was 0.9 nm. The multiplier of the mobility in the Si-rich region was 10,000. (For interpretation of the references to colour in this figure legend, the reader is referred to the web version of this article.)

To understand this in a physically transparent picture, we must regard the asymmetry in the interface sharpness (the width of the two phase regions): where the interface is wider, there are more accessible A (Co or Ni) and B (Si) atoms to be easily pushed into the new phase, which is obviously enough to maintain the temporary asymmetry in the growth rate. Note that this asymmetry is enhanced significantly by an accelerated mobility in the intermetallic phase. This is illustrated in Fig. 10 for the Co–Si system. The figure also shows the theoretical maximum of the difference in thicknesses of the new phases following from our concept. The latter was calculated regarding the conservation of matter: the pure Co and a-Si layers were kept intact, whereas all the Si and Co atoms in the mixture across the two phase regions were incorporated into the intermetallic layers formed at the a-Si/Co and Co/a-Si interfaces.

All these suggest that the combination of two factors, i.e. (i) the initial width of the interfaces (two phase regions) after deposition and (ii) the accelerated mobilities in the intermetallic phase, control the different growth rates of the intermetallic. In consequence, the observed asymmetry in initial growth is clearly a kinetic effect which overrides even the counteracting asymmetry in the driving forces across a thick or thin intermetallic layer.

It is important to note that the suggested model assumes the formation of continuous silicide layers. In principle, other scenarios might also be imagined; for example, the chemical potential of silicide atoms could depend on the layer thickness if the silicide layer consisted of separate islands – the smaller the average island radius, the higher the chemical potential due to capillarity. However, our previous measurements of the Co–Si system using transmission electron microscopy [32] demonstrated the formation of a continuous silicide layer from the very beginning. Accordingly, we based our model on this assumption. Nevertheless, we cannot exclude that alternative concepts based on a particle microstructure or rough interfaces may also lead to a consistent description of the experiments.

5. Conclusions

Present-day technology produces devices structured on the nano- or even atomic scale. Testing these structures and the processes taking place therein often requires nondestructive methods with nanoscale or atomic resolution since destructive counterparts may modify the structures on the same scales. For this reason, development of such methods is highly appreciated. In this work, a combination of in situ XRD and four-wire resistance method as well as a combination of EXAFS and GIXRF measurements in waveguide structure were used to monitor compound phase formation in the Ni–Si system. We further developed the evaluation method by correlating the results obtained from the independent measurements of the GIXRF and EXAFS results. From this, we were able to determine the I_{Ni_2Si}/I_{Ni} ratio as a function of annealing time, which increases the reliability.

Correlating the EXAFS and GIXRF measurements in the waveguide structures and comparing their results, we could follow the very beginning of the phase growth in the metal silicide systems in a non-destructive way. The measurements showed both the appearance and the later development of the Ni_2Si phase; moreover, the GIXRF and EXAFS results showed good correlation. We have shown that, during sample preparation, a disordered or even amorphous Ni_2Si phase formed at both interfaces. This was also supported by a combination of in situ XRD and the four-wire resistance method. However, this phase was thicker when Ni was deposited onto Si than vice versa. This can be explained naturally by the so-called dynamic segregation process. Surprisingly, however, we found that the initially thicker intermetallic phase grows faster than the thinner one. This remarkable behaviour was not only observed in the Ni–Si system, but was also confirmed in the Co–Si system.

To clarify this unexpected phenomenon, we performed computer simulations, which demonstrated that a plausible explanation is that the phase boundaries are more diffuse on the side where the pre-nucleation mixture is thicker initially and the diffusion is accelerated in the intermetallic layer (total mixing mode), which helps the faster initial nucleation there and induces faster phase growth on the same side.

All this suggests that the width of the interfaces (non-equilibrium mixtures across the two phase region) and the accelerated mobilities in the intermetallic phase together determine the kinetics of phase growth and thus the asymmetry in the thickness of the new phases between interfaces of the opposite stacking. It should be noted that the kinetics of the phase growth may depend on the stacking order in bilayer samples.

The initial interface width, which is often directly linked to the deposition order of different components (via dynamic segregation or the effects of ion implantation), and the mobility variation in the system (which influences e.g. the nucleation mode) play key factors in planning and realizing technological processes on the nanoscale.

Acknowledgements

This work was supported by the OTKA Board of Hungary (No. NF101329), and by the TAMOP 4.2.2.A-11/1/KONV-2012-0036 and TAMOP-4.2.2/B-10/1-2010-0024 projects (implemented through the New Hungary Development Plan co-financed by the European Social Fund, and the European Regional Development Fund).

References

[1] F. Hodaj, A. Gusak, Acta Mater. 52 (2004) 4305.
[2] M. Pasichnyy, G. Schmitz, A. Gusak, V. Voyk, Phys. Rev. B (2005) 72.
[3] A. Gusak, T. Zaporozhets, Y. Lyashenko, S. Kornienko, O. Pasichnyy, A. Shirinyan, Diffusion-Controlled Solid State Reactions: in Alloys, Thin-Films, and Nanosystems, John Wiley & Sons, 2010, ISBN 9783527408849.
[4] Z. Erdélyi, G. Schmitz, Reactive diffusion and stresses in spherical geometry, Acta Mater. 60 (4) (2012) 1807–1817.
[5] Z. Erdélyi, C. Cserháti, A. Csik, L. Daróczi, G. Langer, Z. Balogh, et al., X-ray Spectrom. 38 (2009) 338.
[6] C. Lavoie, C. Coia, F.M. d'Heurle, C. Detavernier, C. Cabral, P. Desjardins, et al., Defect Diffus. Forum 237–240 (2005) 825.
[7] A. Tynkova, G.L. Katona, G.A. Langer, S.I. Sidorenko, S.M. Voloshko, D.L. Beke, Beilstein J. Nanotechnol. 5 (2014) 1491.
[8] E. Dudzik, R. Feyerherm, W. Diete, R. Signorato, C. Zilkens, J. Synchrotron Radiat. 13 (2006) 421.
[9] A. Gupta, N. Darowski, I. Zizak, C. Meneghini, G. Schumacher, A. Erko, Spectrochim. Acta B 62 (2007) 622.
[10] A. Gupta, C. Meneghini, A. Saraiya, G. Principi, D. Avasthi, Nucl. Instrum. Methods Phys. Res. B 212 (2003) 458.
[11] B. Dev, A. Das, S. Dev, D. Schubert, M. Stamm, G. Materlik, Phys. Rev. B 61 (2000) 8462.
[12] S. Ghose, B. Dev, A. Gupta, Phys. Rev. B 64 (2001) 233.
[13] L. Parratt, Phys. Rev. 95 (1954) 359.
[14] D. Windt, Comput. Phys. 12 (1998) 360.
[15] S. Ghose, B. Dev, Phys. Rev. B 63 (2001) 245409.
[16] M. Newvill, Fundamentals of XAFS, Consortium for Advanced Radiation Sources, University of Chicago, Chicago, IL, 2004.
[17] G. Vlaic, L. Olivi, Croat. Chem. Acta 77 (3) (2004) 427–433.
[18] F. Fischer, J. Svoboda, Prog. Mater. Sci. 60 (0) (2014) 338–367.
[19] G.B. Stephenson, Acta Metall. 36 (10) (1988) 2663–2683.
[20] T.B. Massalski, H. Okamoto, P.R. Subramanian, L. Kacprzak, Binary Alloy Phase Diagrams, ASM International, Materials Park, 1990.
[21] N. Saunders, A. Miodownik, CALPHAD (Calculation of Phase Diagrams): A Comprehensive Guide, Pergamon Materials Series, Elsevier Science, 1998, ISBN 9780080528434. <http://books.google.hu/books?id=ROnQVsNLZUAC>.
[22] A. Dinsdale, Calphad 15 (4) (1991) 317–425.
[23] T. Tokunaga, K. Nishio, H. Ohtani, M. Hasebe, Calphad 27 (2) (2003) 161–168.
[24] L. Zhang, Y. Du, H. Xu, Z. Pan, Calphad 30 (4) (2006) 470–481.
[25] S. Meschel, O. Kleppa, Standard enthalpies of formation of some 3d transition metal silicides by high temperature direct synthesis calorimetry, J. Alloys Compd. 267 (12) (1998) 128–135.
[26] S. Oukassi, J. Moulet, S. Lay, F. Hodaj, Microelectron. Eng. 86 (2009) 397.
[27] N. Mattoso, J. Mater. Sci. 30 (1995) 3242.
[28] L. Clevenger, C. Thomson, J. Appl. Phys. 67 (1990) 1325.
[29] B. Ravel, M. Newville, J. Synchrotron Radiat. 12 (2005) 537.
[30] P. Villars, Pearson's Handbook: Crystallographic Data for Intermetallic Phases, ASM International, Materials Park, OH, 1997.
[31] M. Ibrahim, Z. Balogh, P. Stender, R. Schlesiger, G.H. Greiwe, G. Schmitz, et al., Acta Mater. 76 (0) (2014) 306–313.
[32] C. Cserháti, Z. Balogh, A. Csik, G.A. Langer, Z. Erdélyi, G. Glodán, et al., J. Appl. Phys. 104 (2) (2008) 024311.